A Self-Decoupled Microstrip Antenna via Inhomogeneous Substrate Manipulation

Yongqi Hu, *Graduate Student Member, IEEE*, Jiangwei Sui, *Member, IEEE*, and Xiangwei Zhu, *Member, IEEE*

***Abstract*—In this article, we introduce a new self-decoupling technique that leverages an inhomogeneous dielectric substrate to significantly suppress the mutual coupling between closely spaced microstrip antennas. Unlike traditional decoupling strategies that rely on modifications of the patch or ground plane, the proposed method achieves self-decoupling by exploring the inhomogeneous substrate manipulation, where the spatial distribution of the substrate's permittivities is deliberately arranged, thereby enabling the mutual cancellation of several distinct coupling paths. The underlying mechanism is revealed through analytical derivation, providing a quantitative guideline for desired designs. To validate the concept, two implementation schemes of the inhomogeneous substrate are investigated. The first scheme (Type I) employs a multicolumn dielectric combination, while the second scheme (Type II) utilizes a monolithic substrate perforated with carefully designed patterns. Several examples for the 1×2, 1×4, and millimeter-wave (mm-wave) scenarios are studied, respectively. The results confirm the superior performance of the proposed approach. To the best of our knowledge, this work constitutes the first demonstration of self-decoupling achieved through substrate permittivity manipulation, and it showcases the potential of additive manufacturing (AM) techniques in the self-decoupling of microstrip antennas.**

***Index Terms*—Inhomogeneous substrate, microstrip antenna, multipath cancellation, self-decoupling, substrate manipulation.**

I. Introduction

To MEET the ever-increasing demands for high-performance wireless systems, multiantenna techniques such as multiple-input multiple-output (MIMO) and in-band full-duplex (IBFD) have emerged as key solutions to address the limitations of single-antenna systems [1]. Among various antenna types, microstrip antennas are particularly attractive for realizing multiantenna systems due to their advantages of low profile, lightweight, and ease of integration. However, the ongoing miniaturization and integration of antenna systems exacerbate the mutual coupling issue in multielement microstrip antennas, leading to degraded efficiency, distorted radiation patterns, and diminished channel capacity [2].

Received 2 October 2025; revised 6 February 2026; accepted 20 February 2026. Date of publication 12 March 2026; date of current version 11 June 2026. This work was supported in part by the National Natural Science Foundation of China under Grant 62201625; in part by Guangdong Basic and Applied Basic Research Foundation under Grant 2025A1515010696; and in part by the Science, Technology and Innovation Commission of Shenzhen Municipality under Grant KJZD20240903101314019. *(Corresponding author: Jiangwei Sui.)*

The authors are with the School of Electronics and Communication Engineering, Sun Yat-sen University, Shenzhen Campus, Shenzhen 518107, China (e-mail: huyq35@mail2.sysu.edu.cn; suijw@mail.sysu.edu.cn; zhuxw666@mail.sysu.edu.cn).

Digital Object Identifier 10.1109/TAP.2026.3671355

Over the past decade, significant research efforts have been dedicated to mitigating mutual coupling in microstrip antenna arrays. Among the proposed techniques, the decoupling network approach [3], [4], [5] offers versatility due to its antenna-type agnosticism. Alternatively, structures such as electromagnetic band gap (EBG) structures [6], [7], and defected ground structures (DGSs) [8], [9], [10], leverage their inherent band-stop or slow wave characteristics to suppress surface current coupling. Similarly, carefully designed parasitic elements [11], [12], [13] can generate counteracting coupling fields. Another effective strategy involves deploying an antenna decoupling surface (ADS) [14], [15] at a height of approximately 0.2–0.3 wavelengths above the antenna plane to introduce a controlled, compensating coupling. Frequency selective surfaces (FSSs) [16], [17] and near-field resonator loading [18] have also demonstrated effective decoupling capabilities. Furthermore, additional compact decoupling structures, including capacitively loaded loops (CLLs) [19], split ring resonators (SRRs) [20], and strategically placed shorting pins [21], have been proposed to enhance port isolation. While these methods achieve appreciable decoupling performance, they invariably require dedicated and often complex structures, which may increase the overall system complexity or physical footprint of the antenna system.

In contrast, self-decoupling schemes exploit intrinsic antenna properties to enhance isolation without external structures, offering inherent advantages in compactness and integration. These approaches primarily manifest in the following forms.

1) *Weak-Field Region Construction:* Decoupling is achieved by creating localized field minima at the coupled antenna's feed point. This can be realized through patch-layer modifications (e.g., inset feed lines [22]) or ground-plane-layer manipulations (e.g., optimized ground plane dimensions [23]).
2) *Mode Superposition:* Isolation is attained by exciting and superposing specific different modes with opposite phases. Techniques include manipulating TM_{01} and TM_{11} modes via metallic vias/cuts [24] or corner truncation [25], counteracting TM_{10} and TM_{02} modes using engineered slots [26] or meandered patch edges [27], and canceling characteristic modes via differential feeding [28]. Extending this principle, wideband decoupling exploits multiple-mode excitation and superposition [29]. These methods predominantly involve patch-layer adjustments.

3) *Differential/Common-Mode (CM/DM) Cancellation:* Effective decoupling is achieved by regulating CM and DM signals. Strategies include connecting decoupling inductors for mutual signal cancellation [30], adjusting feed height [31], or employing grounded coupling posts for impedance control [32].
4) *Hybrid Mode Exploitation:* Natural cancellation occurs between hybrid modes, such as monopole and patch modes [33], inverted-F and patch modes [34], or L-probe and patch modes [35]. Notably, a recent concept achieves efficient coupling cancellation by strategically adjusting the patch geometry to balance the electric and magnetic coupling components [36].

In summary, conventional microstrip antenna decoupling techniques typically employ the following three approaches: 1) introducing well-designed decoupling structures above the radiating patch; 2) exploring and optimizing the patch-layer geometry; or 3) integrating slot configurations on the ground plane.

These methods introduce inherent tradeoffs: elevated structures increase profile height, patch modifications usually enlarge antenna dimensions, and ground-plane slots can exacerbate backward radiation. In contrast, dielectric substrate manipulation offers a fundamentally distinct pathway to microstrip antenna decoupling that inherently circumvents these limitations. Crucially, no prior work has demonstrated self-decoupling through deliberate substrate manipulation.

Furthermore, additive manufacturing (AM), also known as 3-D printing, has emerged as a transformative solution for antenna fabrication. Experimental validations [37], [38], [39], [40] demonstrate the feasibility of implementing 3-D printing in antenna production to produce the desired dielectric substrate. However, existing designs primarily focus on performance improvements for the single-element microstrip antenna, such as polarization and radiation patterns. To date, no prior work has investigated the application of 3-D printed dielectric substrates for microstrip antenna decoupling.

In this article, a new self-decoupling method is proposed for microstrip antennas based on inhomogeneous substrate manipulation. The proposed approach leverages the permittivity distribution of the substrate to counteract multipath couplings. Two types of inhomogeneous substrates are proposed: Type I involves integrating multiple dielectrics with different permittivity, while Type II involves perforating a multicolumn lattice on a homogeneous dielectric to achieve an equivalent permittivity distribution. For practical implementation, 3-D printing is adopted to fabricate the Type-II inhomogeneous substrate. Compared to prior decoupling techniques for microstrip antennas, the proposed method offers two key contributions: 1) it is the first time to achieve self-decoupling of microstrip antennas through substrate permittivity manipulation and 2) it exploits 3-D printing to implement the inhomogeneous dielectric substrate for self-decoupling.

This article is organized as follows. The working mechanisms are presented in Section II. Section III presents the Type-I self-decoupled microstrip antenna design, followed by the second Type-II design in Section IV. Finally, conclusions are given in Section V.

II. Working Mechanism

A. Self-Decoupling: Multipath Coupling Cancellation

Fig. 1 illustrates the design evolution of the proposed self-decoupling scheme employing an inhomogeneous substrate. As depicted in Fig. 1(a), the traditional reference microstrip antenna typically comprises three distinct layers: the top radiating microstrip patch, the middle dielectric substrate, and the bottom ground plane. Conventionally, this substrate is homogeneous, featuring uniform material composition and geometry, and its relative permittivity is denoted as ε_{r0}. As the S-parameters show, significant mutual coupling is observed in this reference antenna within the 3.4–3.6 GHz band.

To mitigate this undesired mutual coupling, a self-decoupled microstrip antenna, denoted as Type I, is proposed in Fig. 1(b). In this design, the original homogeneous substrate in Fig. 1(a) is replaced by an inhomogeneous one composed of two columns with distinct relative permittivity values, ε_{r1} and ε_{r2}. Without loss of generality, the following analysis assumes that ε_{r1} is supposed to be larger than ε_{r2}. To ensure its resonant and radiation characteristics are comparable to the reference conventional antenna with homogeneous dielectric, the equivalent relative permittivity should satisfy the half-wavelength electrical length condition along the longitudinal direction (y-axis), expressed as follows:

$$\frac{1}{\sqrt{\varepsilon_{re1}}}+\frac{1}{\sqrt{\varepsilon_{re2}}}\approx\frac{2}{\sqrt{\varepsilon_{re0}}}. \tag{1}$$

Here, ε_{re1}, ε_{re2}, and ε_{re0} are the effective permittivities corresponding to ε_{r1}, ε_{r2}, and ε_{r0}, respectively, and are given by

$$\varepsilon_{re}=\frac{\varepsilon_r+1}{2}+\frac{\varepsilon_r-1}{2}\left(1+12\frac{h}{w_t}\right)^{-1/2} \tag{2}$$

where h is the substrate thickness, and w_t is the transmission linewidth. In the antenna array arranged along the H-plane, w_t corresponds to the patch length.

Along the x-axis, the inhomogeneous substrate introduces two distinct coupling components, denoted as k_1 and k_2, where k_1 depends strongly on ε_{r1} and k_2 on ε_{r2}, as depicted in Fig. 1(b). It is understood that k_1 and k_2 are determined by the current distributions on the two patches, which include the current intensities and the equivalent electrical distance between the two current distributions on the two patches. In this sense, k_1 and k_2 can be formulated as follows:

$$k_1\propto f\left(I_1\left(x,y\right),l_1\right) \tag{3a}$$

$$k_2\propto f\left(I_2\left(x,y\right),l_2\right) \tag{3b}$$

where I_1 and I_2 denote the current intensities on the two halves of the patch, which are functions of the position, and l_1 and l_2 denote the equivalent electrical distance between the two current distributions. Since the dielectric substrates with distinct permittivity values exhibit differentiated electrical lengths, k_1 and k_2 will present different characteristics. For I_1 and I_2, considering the patch symmetry, the average current intensities on the two halves can be regarded as comparable, so the magnitudes of k_1 and k_2 can also be regarded as comparable. In contrast, for l_1 and l_2, due to the substrate permittivity difference of the two halves, the equivalent electrical distances

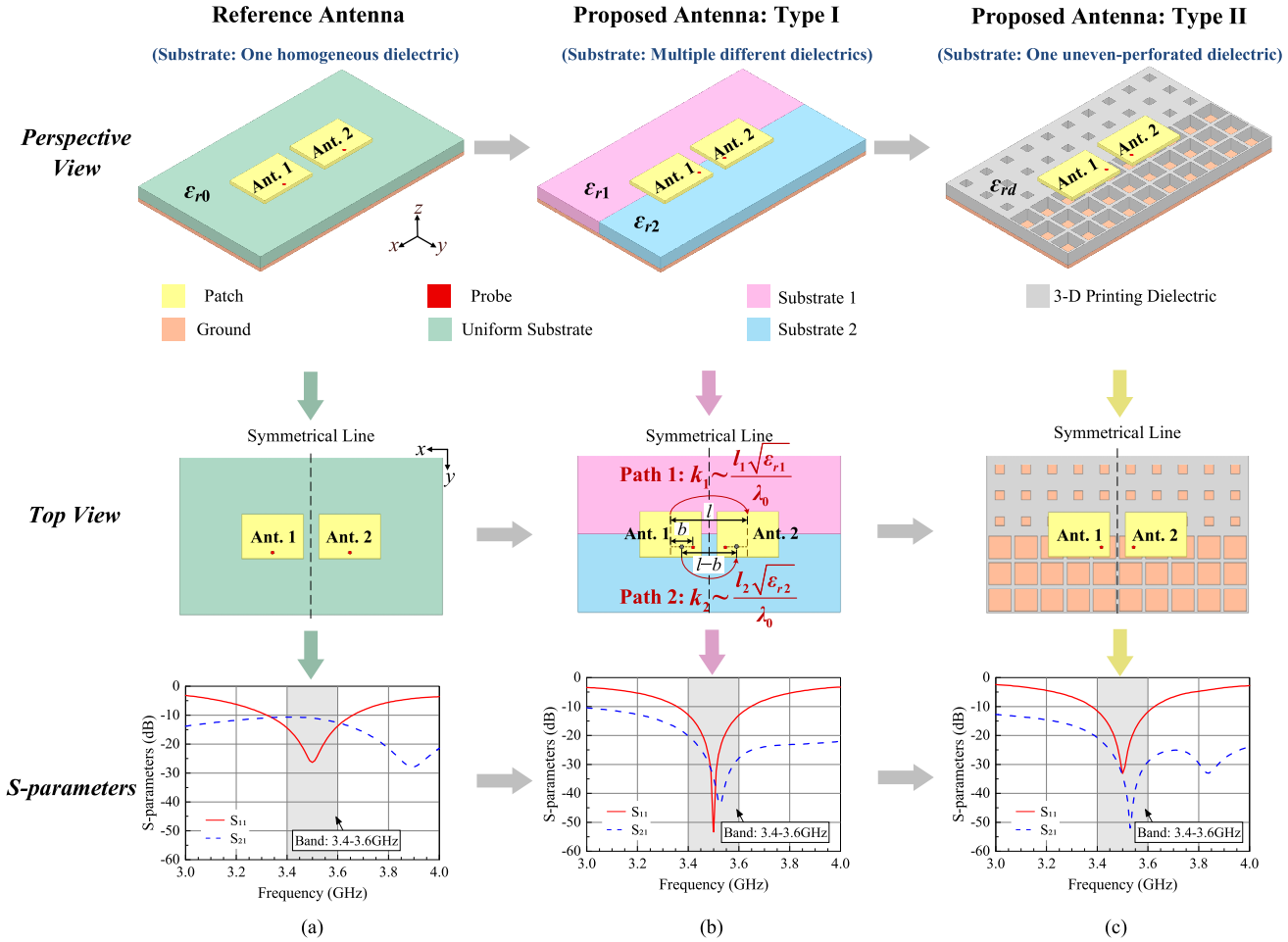

Fig. 1. Antenna configuration evolution of the proposed self-decoupling scheme by manipulating inhomogeneous substrate. (a) Reference antenna with one homogeneous substrate. (b) Proposed antenna with inhomogeneous substrate of different permittivity: Type I. (c) Proposed antenna with inhomogeneous substrate of different perforation size: Type II.

differ greatly, so the phase of k_1 and k_2 can be effectively manipulated. In summary, the underlying decoupling mechanism is to counteract the two kinds of coupling, k_1 and k_2, out of phase with each other by controlling the equivalent electrical distance through permittivity manipulation.

Moreover, the off-center feeding along the x-axis is introduced to suppress cross-polarization, as will be elaborated subsequently. Taking the current distribution unevenness caused by the off-center feeding, the equivalent center point to calculate l_2 is set as the middle point between the patch center point and the feeding point for calculating k_2, as denoted in Fig. 1(b). Differently, for the upper half, the current distribution unevenness is much less compared with the lower half, so the equivalent center point to calculate l_1 is just set as the patch center point. Therefore, l_2 can be derived as follows:

$$l_2 = l_1 - b \tag{4}$$

where b is the offset of the feeding point from the patch center along the x-axis.

To make the two coupling paths cancel each other out, an anti-phase relationship between k_1 and k_2 should be satisfied, expressed as follows:

$$\frac{2\pi l_1}{\lambda_0}\sqrt{\varepsilon_{re1}} - \frac{2\pi l_2}{\lambda_0}\sqrt{\varepsilon_{re2}} \approx \pi \tag{5}$$

where λ_0 denotes the free-space wavelength at the operation frequency.

By simultaneously solving (1) and (5), and substituting the results into (2), the combination of permittivities for the inhomogeneous substrate required to achieve self-decoupling can be inversely derived. It is worth noting that while the presented equations capture the primary decoupling mechanism, they serve mainly as a guide for the initial design, and further fine-tuning and optimization are required to obtain a better performance. Together, the phase opposition and amplitude balance lead to an inherent mutual coupling cancellation between k_1 and k_2, as proved by the significant reduction in S_{21} shown in Fig. 1(b). It is noteworthy that this decoupling mechanism is extensible: a four-column configuration can be developed from the two-column design through performance-driven optimization.

However, fabricating the Type-I substrate shown in Fig. 1(b) by integrating different dielectric materials with specific permittivities poses significant practical challenges. To address this implementation issue, we propose a second type of inhomogeneous substrate, designated as Type II, which emulates the functionality of Type I using a single dielectric material. This approach leverages the principle that perforating a dielectric can effectively modulate its equivalent relative permittivity

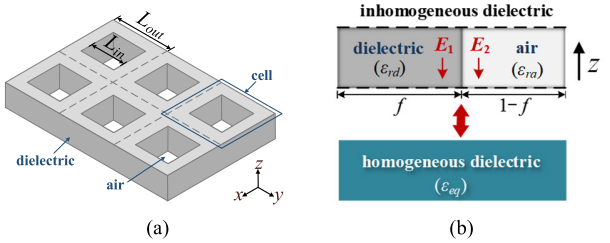

Fig. 2. Geometry and equivalent model of the proposed Type-II inhomogeneous substrate. (a) Geometry. (b) Equivalent model.

[41], [42]. As depicted in Fig. 1(c), the Type-II design generates distinct dielectric regions by introducing perforations with varied dimensions and spacing into a uniform substrate. Crucially, unlike the Type-I antenna in Fig. 1(b), the inhomogeneity of the Type-II substrate arises from constructing each column with building cells of different dimensions. Each building cell is formed by removing a right square prism from the original solid substrate, resulting in a hollow basic cell. By controlling the size of this excised square prism, the equivalent relative permittivity of the remaining cell can be correspondingly manipulated. This allows the equivalent permittivities of the two columns in the Type-II antenna to be engineered to match the material permittivities of the Type-I design. Therefore, a similar decoupling effect can be achieved, as confirmed by the simulated S-parameters in Fig. 1(c). In essence, while both designs rely on inhomogeneous substrates, Type I uses material diversity, whereas Type II employs structural diversity. The use of a single material makes the Type-II antenna a more flexible and practical solution for fabrication.

B. Relative Permittivity Equivalence Between Homogeneous and Perforated Substrates

This section investigates the equivalent mechanism of the proposed Type-I and Type-II inhomogeneous substrates. For reasons of structural symmetry and fabrication simplicity, the design employs a specific building cell: a right square prism of dielectric material, perforated by a concentric, square, air-filled void. As depicted in Fig. 2(a), the artificial inhomogeneous substrate is formed by periodically arranging these building cells. To estimate the effective permittivity, a simplified analytical model is shown in Fig. 2(b). Within the substrate of a microstrip antenna, the electric field is predominantly oriented in the vertical direction, normal to the ground plane. Consequently, the electric field runs parallel to the dielectric-air interface. According to electromagnetic boundary conditions, the tangential component of the electric field strength $\boldsymbol{E}$ must remain continuous across the interface

$$E_1 = E_2 \tag{6}$$

where E_1 and E_2 are the tangential components of the electric field strengths in the dielectric and air, respectively.

Since the average electric field and polarization of an inhomogeneous dielectric are identical to those of its equivalent homogeneous dielectric [44], that is,

$$E_{eq} = fE_1 + (1-f)E_2 \tag{7}$$

$$P_{eq} = fP_1 + (1-f)P_2 \tag{8}$$

where E_{eq} and P_{eq} are the electric field strength and polarization density of the equivalent homogeneous dielectric, respectively, with f denoting the filling factor of the dielectric. Based on the constitutive relation $P = \varepsilon_0(\varepsilon_r - 1)E$, (8) can be reformulated as follows:

$$\varepsilon_{eq}E_{eq} = f\varepsilon_{rd}E_1 + (1-f)\varepsilon_{ra}E_2 \tag{9}$$

where ε_{eq}, ε_{rd}, and ε_{ra} are the relative permittivity of the equivalent substrate, the dielectric, and the air, respectively.

By substituting (7) into (9), the effective relative permittivity of the perforated substrate can be expressed as follows:

$$\varepsilon_{eq} = \frac{f\varepsilon_{rd}E_1 + (1-f)\varepsilon_{ra}E_2}{fE_1 + (1-f)E_2}. \tag{10}$$

Given that $E_1 = E_2$ in (6), (10) is reducible to

$$\varepsilon_{eq} = f \cdot \varepsilon_{rd} + (1-f)\,\varepsilon_{ra}. \tag{11}$$

The filling factor f can be derived from the geometric parameters illustrated in Fig. 2(a)

$$f = \frac{L_{out}^2 - L_{in}^2}{L_{out}^2} \tag{12}$$

where L_{out} and L_{in} are the lengths of the building cell and air hole, respectively.

Notably, by adjusting these geometric parameters, the dielectric-to-air volume ratio can be controlled to modulate the effective relative permittivity of the perforated dielectric substrate. The calculated results from (11) exhibit excellent agreement with resonant cavity measurements [45], demonstrating the validity of evaluating the effective relative permittivity of the proposed Type-II inhomogeneous substrate.

III. Self-Decoupled Antenna With Inhomogeneous Substrate: Type I

A. Antenna Configuration

Fig. 3(a) shows two H-plane coupled microstrip patch antennas operating in the band from 3.4 to 3.6 GHz, separated by an edge-to-edge spacing D of 6 mm ($0.07\lambda_0$, where λ_0 is the free-space wavelength at 3.5 GHz). The probe-fed patches are implemented on a homogeneous dielectric substrate ($\varepsilon_{r0} = 4.8$, $\tan\delta = 0.01$), with feeding probes offset by a distance a from the patch centers along the y-axis. Taking into consideration the eventual fabrication, the radiating elements and ground plane are 0.5 mm thick. Typically, dielectric polarization currents induce strong radiation in directions along the ground plane, leading to a strong coupling between the antenna elements [46].

According to the mechanism analysis in the last part, by tailoring the permittivity distribution of the substrate, multipath coupling in the inhomogeneous dielectric substrate can be counteracted to achieve a natural high isolation. To validate the proposed self-decoupling scheme, a two-column dielectric self-decoupled antenna is presented, as illustrated in Fig. 3(b). This design integrates two substrates (Substrate 1 and Substrate 2) with equal dimensions but distinct relative permittivity (ε_{r1} and ε_{r2}) to form a two-column inhomogeneous dielectric

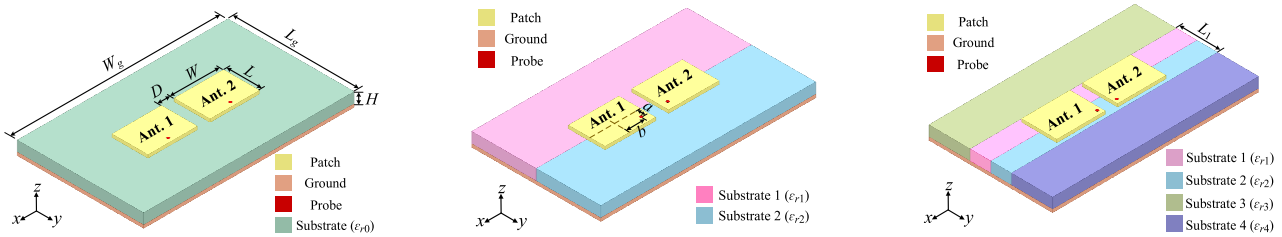

Fig. 3. Antenna configurations of the reference antenna and the proposed Type-I antenna. (a) Reference coupled antenna with one homogeneous substrate. (b) Proposed Type-I antenna with two-column substrates. (c) Proposed Type-I antenna with four-column substrates. The detailed dimensions are W = 23.5 mm, L = 17.1 mm, W_g = 140 mm, L_g = 60 mm, H = 5 mm. ε_{r0} = 4.8, a = 6.4 mm for (a), ε_{r1} = 8, ε_{r2} = 3, a = 5 mm, b = 8.6 mm for (b), and ε_{r1} = 8, ε_{r2} = 3.4, ε_{r3} = 3.2, ε_{r4} = 3.8, a = 6.4 mm, b = 10 mm, L_1 = 20 mm for (c).

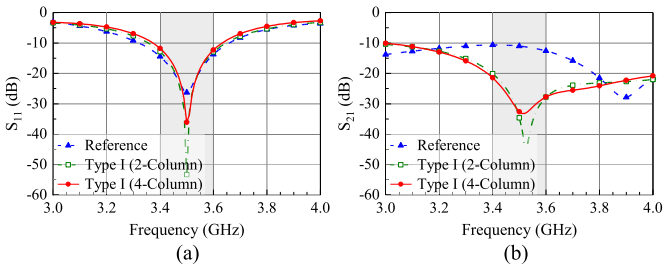

Fig. 4. Simulated S-parameters of the coupled and proposed Type-I self-decoupled antennas. (a) S_{11}. (b) S_{21}.

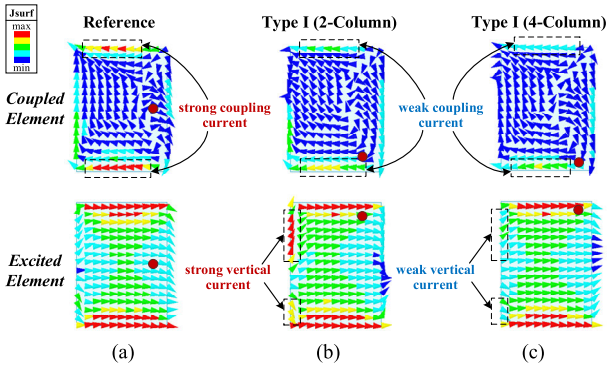

Fig. 5. Simulated current distribution on the surface of the patches with port 1 excitation. (a) Reference coupled antenna. (b) Proposed self-decoupled Type-I antenna with two-column substrates. (c) Proposed self-decoupled Type-I antenna with four-column substrates. The red circle dots denote the ports.

substrate. Unlike traditional microstrip antenna, the proposed antenna employs an offset feeding strategy relative to the transverse centerline of the patch. This asymmetrical excitation is specifically designed to compensate for cross-polarization deterioration induced by substrate inhomogeneity. According to (1)–(5), for b = 8.6 mm and ε_{r0} = 4.8, the ε_{r1} and ε_{r2} can be calculated as 8.59 and 2.99, respectively, which are close to the final optimized values of 8 and 3. It is observed that a good agreement is achieved, demonstrating the effectiveness of the above mechanism analysis.

To enhance parametric tuning flexibility and optimize self-decoupling performance, the two-column dielectric substrate is augmented to a four-column configuration with distinct relative permittivities, as illustrated in Fig. 3(c). This configuration preserves geometric symmetry, with Substrates 1 and 2 and Substrates 3 and 4 maintaining equal widths within the respective pairs. Crucially, Substrates 1 and 2, positioned beneath the patch, exert the dominant influence on antenna characteristics. Compared to the two-column implementation, this four-column dielectric substrate introduces three additional tunable parameters (ε_{r3}, ε_{r4}, and L_1) and expands the coupling paths from two to four. Proper permittivity modulation of the four dielectric columns enables four coupling paths to cancel out with each other, effectively enhancing the isolation. Notably, these three antennas share the same patch size (L, W), patch separation (D), and substrate size (L_g, W_g, H).

B. Decoupling Performance

As illustrated in Fig. 4, all these antennas achieve reflection coefficients (S_{11}) below −10 dB within the target 3.4–3.6 GHz band, demonstrating satisfactory impedance matching. With a $0.07\lambda_0$ edge-to-edge spacing, the reference coupled antenna with a homogeneous substrate exhibits an isolation between 10.7 and 12.6 dB. Significantly, the Type-I antenna with a two-column substrate achieves an isolation better than 20.1 dB ($S_{21} < -20.1$ dB), providing an improvement of 9.5–32.1 dB (peaking at 32.1 dB at 3.52 GHz) compared to the reference antenna. Extending this configuration to the inhomogeneous four-column substrate in Fig. 3(c) further elevates the isolation above 21.5 dB.

Fig. 5 shows the vector current distributions on the patch surface of the three antennas when Port 1 is excited. In the reference coupled case, electromagnetic waves radiated by Ant. 1 induce strong coupling currents on Ant. 2. In contrast, for the two proposed Type-I antennas, the current magnitude on Ant. 2 is significantly suppressed. Furthermore, a comparative analysis reveals that the four-column dielectric design holds a distinct advantage. By effectively suppressing the undesired cross-polarized current components on the excited patch surface, the four-column configuration achieves lower cross-polarization and enhanced polarization purity compared to its two-column counterpart. This improvement is further confirmed by the following simulated radiation patterns.

As illustrated in Fig. 6, while both the two-column and four-column antennas successfully restore the H-plane radiation pattern in the boresight direction, they exhibit different levels of cross-polarization. Notably, the two-column

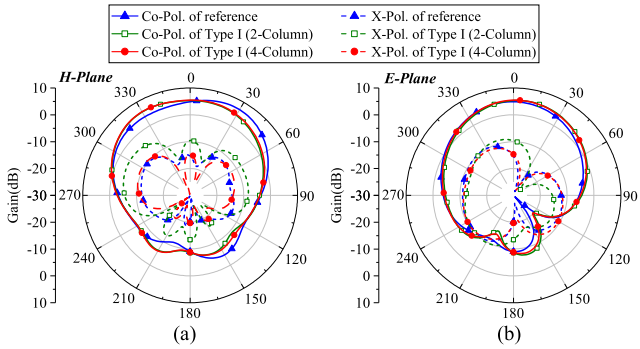

Fig. 6. Simulated radiation patterns of the proposed self-decoupled Type-I antennas and the reference coupled one at 3.5 GHz. (a) H-plane. (b) E-plane.

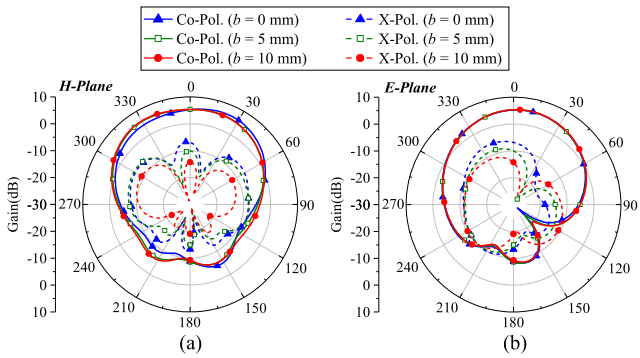

Fig. 7. Simulated radiation patterns of the proposed four-column dielectric antenna at 3.5 GHz with the variation of b. (a) H-plane. (b) E-plane.

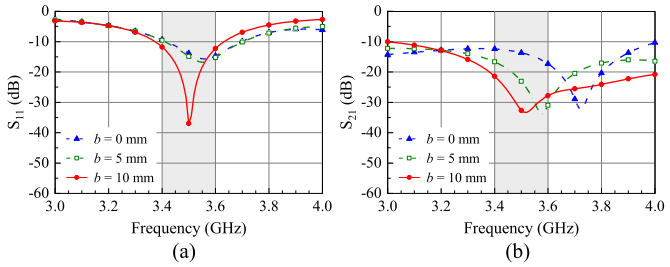

Fig. 8. Simulated S-parameters of the proposed four-column dielectric antenna with the variation of b. (a) S_{11}. (b) S_{21}.

configuration degrades cross-polarization compared with the reference coupled one. Conversely, by leveraging the extra tunable parameters in the four-column design, the cross-polarization can be suppressed to a level comparable to that of the reference one. This demonstrates that the proposed Type-I substrate can enable self-decoupling while preserving the radiation pattern characteristics.

The effects of the off-center feeding are worthy of further investigation. Taking the feeding offset in Fig. 3(c) as a representative case, its impact on both cross-polarization and isolation performance is studied, as indicated by the radiation patterns and S-parameters shown in Figs. 7 and 8. It is observed that regarding cross-polarization performance, b exerts a significant regulatory effect. As b increases, the cross-polarization levels in both the H- and E-planes exhibit an obvious decline, particularly in the boresight direction. At b = 10 mm, the cross-polarized component is effectively

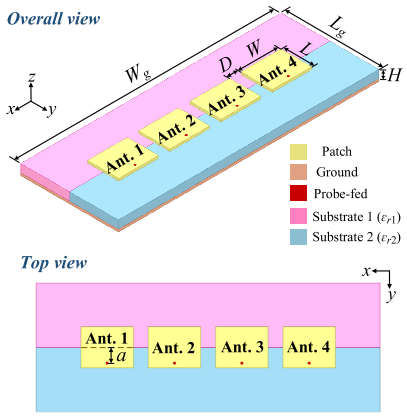

Fig. 9. Configurations of the proposed center-fed 1 × 4 array. The detailed dimensions are W = 24.4 mm, L = 19.1 mm, W_g = 190 mm, L_g = 60 mm, H = 5 mm, D = 7 mm, a = 7.3 mm, ε_{r1} = 8, and ε_{r2} = 2.6.

suppressed to a low level of −9.1 dB. Thus, different from the traditional microstrip antenna with a homogeneous substrate, the proposed off-center feeding compensates for the asymmetry from nonuniform dielectric distribution, acting as an effective solution to restore the polarization purity of the antenna.

In addition to the effect on the polarization purity, the off-center feeding can also help tune the decoupling frequency by modifying the equivalent electrical distance, l_2, as has been discussed in Section II-A. It is observed from Fig. 8 that as b increases, the impedance matching bandwidth remains almost unchanged. Notably, the transmission zero of S_{21} exhibits a distinct shift toward lower frequencies as b increases. This phenomenon is attributed to the increased coupling path length difference as b grows. Therefore, the feeding position can also help tune the decoupling frequency through the synergistic cooperation between the off-center feeding and the substrate manipulation.

C. 1 × 4 *Antenna Array*

To explicitly demonstrate the scalability capability of the proposed scheme, a 1 × 4 antenna array is further studied, as shown in Fig. 9.

As shown in Fig. 9, four elements share identical dimensions and feeding positions, with feeding points located on the centerline of the patch width. Fig. 10 compares the simulated S-parameters of the proposed array against a reference array with identical dimensions and feeding positions but utilizing a homogeneous substrate (ε_{r0} = 4). It is seen that the −10-dB impedance bandwidths of all ports successfully cover the target 3.4–3.6 GHz band, and mutual coupling between adjacent elements is significantly suppressed to below −18.6 dB. Compared to the reference array, in-band isolation is enhanced by 7.7–28.3 dB. For nonadjacent elements, isolation remains above 20 dB. However, it should be noted that due to the inherent asymmetry of the inhomogeneous substrate, the cross-polarization levels for each element are a little high, and off-center feeding can be adopted to further optimize the cross-polarization performance.

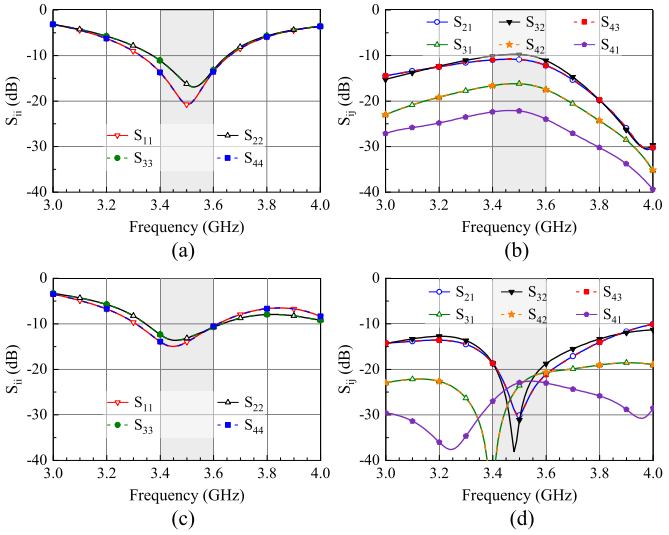

Fig. 10. Simulated S-parameters. (a) S_{ii} and (b) S_{ij} of the reference array. (c) S_{ii} and (d) S_{ij} of the proposed center-fed 1×4 array.

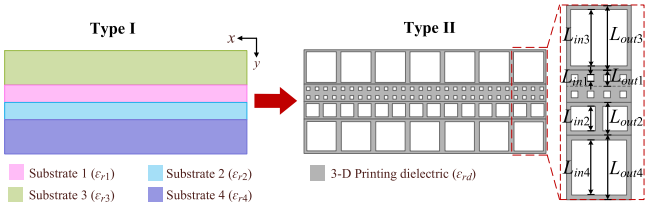

Fig. 11. Model of the proposed Type-I inhomogeneous substrate with four columns and its equivalent Type-II inhomogeneous substrate.

TABLE I
INITIAL DIMENSIONS OF THE TYPE-II PERFORATED SUBSTRATE

Substrate Number	Effective ε_{eq}	Cell Size (L_{out}), mm	Hole Size (L_{in}), mm
3	3.2	20	17.03
1	8	5	1.77
2	3.4	10	8.37
4	3.8	20	16.12

IV. SELF-DECOUPLED ANTENNA WITH INHOMOGENEOUS SUBSTRATE: TYPE II

A. Antenna Configuration

As previously discussed, single dielectric substrates with square holes of varying dimensions are employed to equivalently replace the multidielectric integrated substrates, as illustrated in Fig. 11. The targeted equivalent relative permittivities are achieved by controlling the hole size within each specific building cell to regulate the filling ratio f in (11). Alumina (Al_2O_3), a ceramic material with high permittivity and low loss, is selected as the 3-D printed substrate material due to its ability to achieve the requisite relative permittivity range. The simulated alumina material has a relative permittivity (ε_{rd}) of 9 and a loss tangent (tan δ) of 0.0004. With the relative permittivity of air $\varepsilon_{ra} = 1$, (11) and (12) enable

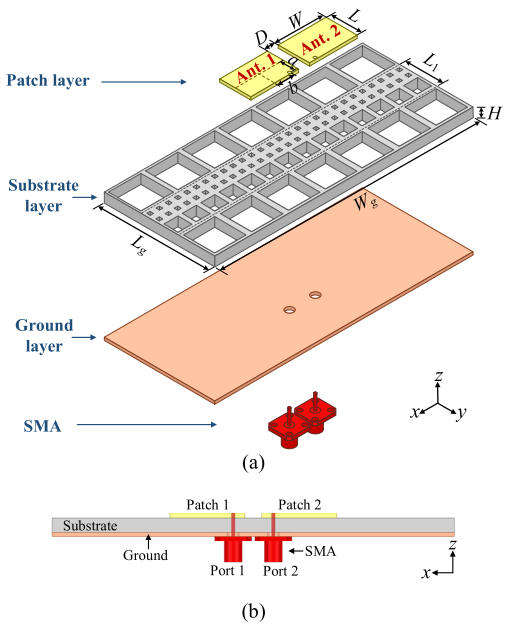

Fig. 12. Antenna configuration of the proposed Type-II antenna. (a) Teardown view. (b) Side view. The dimensions of the antennas are $W = 26$, $L = 16.8$, $W_g = 140$, $L_g = 60$, $H = 5$, $a = 7.5$, $b = 9$, $L_1 = 20$, $L_{out1} = 5$, $L_{in1} = 2$, $L_{out2} = 10$, $L_{in2} = 7.6$, $L_{out3} = 20$, $L_{in3} = 17.6$, $L_{out4} = 20$, and $L_{in4} = 17$ (Unit: mm).

the determination of building cell and hole dimensions for each column of the four-column inhomogeneous dielectric substrate, as given in Table I. It should be mentioned that the relatively large dimensions of building cells introduce a nonideal effective permittivity distribution to some extent, resulting in small discrepancies between theoretical model predictions and simulation results. Therefore, fine-tuning of the dimension is also required to achieve the desired performance. Fig. 12 depicts the complete geometry of the Type-II self-decoupled antenna, where the original four-column inhomogeneous substrate of the Type-I design is realized with the substrate featuring nonuniform perforations shown in Fig. 11.

However, mechanical drilling imposes stringent constraints on minimum aperture size and pitch, which can easily lead to material fracture. Furthermore, conventional subtractive manufacturing techniques not only restrict achievable hole geometries but also prove labor-intensive and time-consuming. To address these limitations, this article employs 3-D printing for perforated substrate fabrication, enabling rapid prototyping and enhanced design flexibility. Therefore, in the simulation, the manufacturing precision of 3-D printing becomes another critical factor to be considered when modifying the dimensions of the Type-II substrate. Given the 0.6-mm-diameter printing nozzles, a minimum wall thickness of 1.2 mm is mandated to maintain structural integrity. Following the dimensional adaptations of the cells and holes, further optimization of the patch dimensions and feeding position is required.

B. Decoupling Performance

Fig. 13 compares the simulated S-parameters of the reference coupled antenna and the two types of self-decoupled

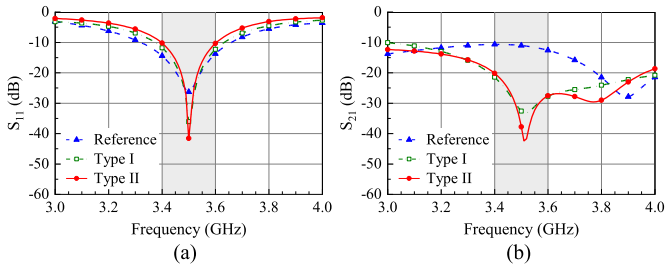

Fig. 13. Simulated S-parameters of the coupled antenna and two proposed self-decoupled antennas: Type I and Type II. (a) S_{11}. (b) S_{21}.

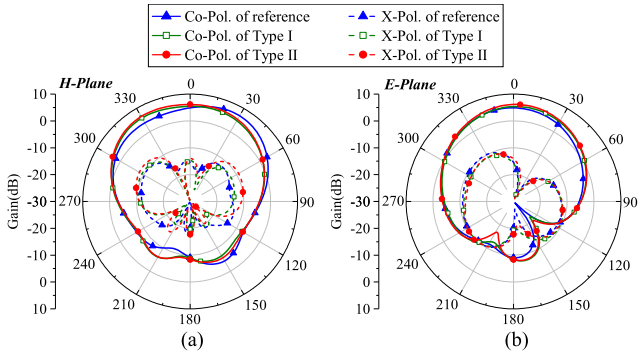

Fig. 14. Simulated radiation patterns of two proposed self-decoupled and the coupled antennas at 3.5 GHz. (a) H-plane. (b) E-plane.

antennas, Type I and Type II. The Type-II design demonstrates an isolation exceeding 20.2 dB across the 3.4–3.6 GHz band. This represents a significant enhancement over the reference antenna, with a maximum improvement of 31.3 dB achieved at 3.51 GHz. Moreover, a comparison of the Type-I and Type-II results reveals that replacing the multimaterial inhomogeneous substrates with a homogeneous one featuring nonuniform perforations has a negligible influence on impedance matching and decoupling performance within the operational band.

Fig. 14 compares the simulated radiation patterns of the reference antenna and the two types of self-decoupled antennas when Port 1 is excited. Compared with the reference antenna, the Type-II antenna effectively corrects distortions in the H-plane pattern. Furthermore, the transition from Type I to Type II maintains consistent radiation patterns while having a negligible effect on cross-polarization.

C. Experimental Validation

Fig. 15(a) shows the fabricated prototype of the 3-D printed alumina substrate with nonuniform perforations. The four kinds of distinct square perforations are clearly visible. The substrate was fabricated via powder extrusion printing (PEP), an indirect ceramic 3-D printing technique combining AM with powder metallurgy. The PEP process involves extruding powder-binder feedstock to form a green body, followed by debinding and sintering to yield a final densified component. The assembled prototype of the proposed self-decoupled antenna using the 3-D printed substrate is presented in Fig. 15(b), with both the patch and ground plane fabricated from 0.5-mm-thick brass sheets. Two quad-flange SMA connectors with 50-Ω characteristic impedance serve as the

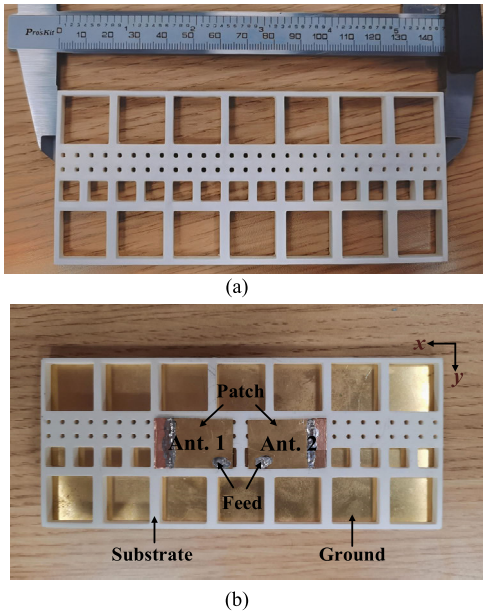

Fig. 15. Pictures of the fabricated Type-II self-decoupled antenna. (a) 3-D printed substrate. (b) Whole integrated antenna.

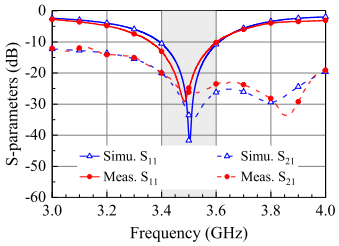

Fig. 16. Simulated and measured S-parameters of the proposed 3-D printed self-decoupled antenna.

feed interfaces. Owing to potential 3-D printing inaccuracies and variations in the permittivity of the alumina material, the final antenna dimensions were fine-tuned based on empirical measurements.

The measured S-parameters after dimension optimization are presented in Fig. 16, exhibiting close agreement with simulated results. The measured and simulated −10-dB S_{11} impedance bandwidths span 3.36–3.60 GHz (6.9%) and 3.395–3.61 GHz (6.1%), respectively. Within the targeted 3.4–3.6 GHz band, the proposed antenna achieves high isolation exceeding 20 dB, alongside satisfactory impedance matching ($S_{11} < -10$ dB).

Fig. 17 shows the measured radiation patterns of the 3-D printed self-decoupled antenna at the center frequency of 3.5 GHz under Port 1 excitation. The measured results are in good agreement with the simulations, except for minor discrepancies in backward radiation, which may be attributable to measurement uncertainty. Both patterns exhibit strong broadside radiation characteristics, with cross-polarization levels remaining below −8 dB in the principal planes.

Fig. 18 presents the measured total efficiency of the 3-D printed self-decoupled antenna when Port 1 is excited. Within the band, the total efficiency ranges from 80% to 96%.

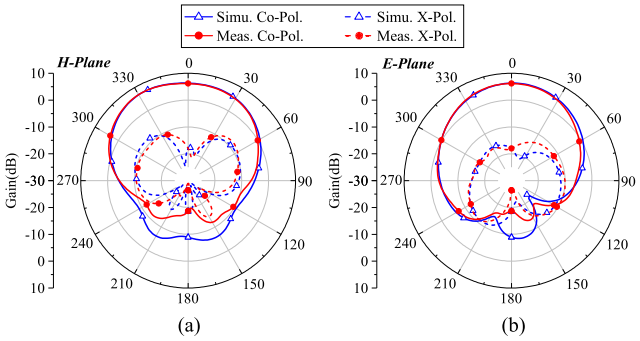

Fig. 17. Simulated and measured radiation patterns of the 3-D printed self-decoupled antenna at 3.5 GHz. (a) H-plane. (b) E-plane.

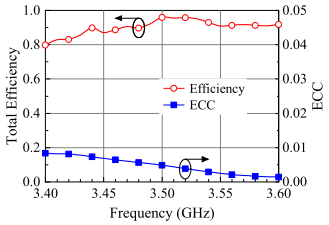

Fig. 18. Measured total efficiency and calculated ECCs of the 3-D printed self-decoupled antenna.

This high efficiency is attributed not only to the low-loss characteristics of the alumina ceramic substrate but also to the excellent impedance matching and high port isolation of the antenna. Furthermore, Fig. 18 also plots the in-band envelope correlation coefficients (ECCs), which were calculated from the measured far-field electric fields. With ECCs below 0.0084 across the band, it demonstrates exceptionally low pattern correlation and excellent diversity characteristics, suggesting high-performance spatial multiplexing.

D. Wideband Self-Decoupled Design

To enhance the impedance bandwidth of that in Fig. 16, a substrate-integrated Π-type matching network is incorporated beneath the proposed Type-II antenna, resulting in the wideband configuration shown in Fig. 19. Fig. 20 presents two pictures of the fabricated prototype. The measured S-parameters are presented in Fig. 21. Good agreement is observed between the simulated and measured results, with minor discrepancies attributed to fabrication tolerances and measurement errors. The optimized design maintains a reflection coefficient below −10 dB across the 3.3–3.8 GHz band, with measured isolation consistently above 18.2 dB, validating the effectiveness of the wideband decoupling.

E. Comparison and Discussions

In Table II, the proposed self-decoupling scheme for two microstrip antennas is compared with existing self-decoupling methods. First, from a comparative analysis of the manipulated parts, it is evident that the existing approaches predominantly rely on radiator characteristics [25], [26], [30], [36], typically through patch geometry modifications to control two resonant modes or adjust electric and magnetic coupling weights to

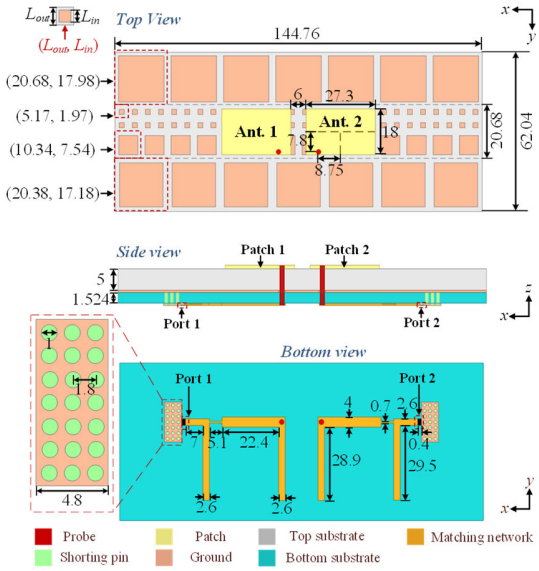

Fig. 19. Configuration of the wideband 3-D printed self-decoupled antenna (Unit: mm).

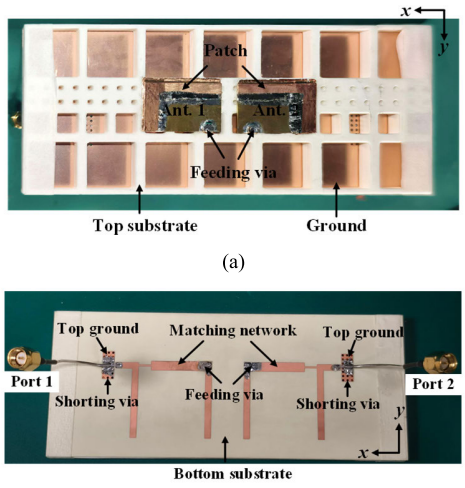

Fig. 20. Pictures of the fabricated Type-II wideband self-decoupled antenna. (a) Top view. (b) Bottom view.

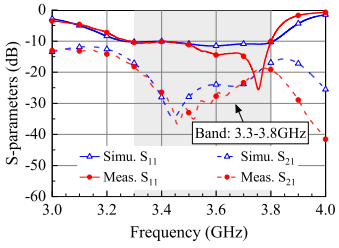

Fig. 21. Simulated and measured S-parameters of the proposed wideband 3-D printed self-decoupled antenna.

generate a transmission zero. Furthermore, certain designs optimize feeding structures [22] or leverage ground plane characteristic modes [23] to create weak field regions. Collectively, existing self-decoupling solutions focus on three key parts: the

TABLE II
COMPARISONS OF THE PROPOSED AND THE PREVIOUS SELF-DECOUPLED MICROSTRIP PATCH ANTENNA

Ref.	Manipulated part	Center frequency (GHz)	Center-to-center Spacing (λ_0)	Profile (λ_0)	Usable bandwidth*	Isolation Increase**(dB)	Total Efficiency
[22][2020]	Feeding structure	3.5	0.5	0.037	3.4% (3.43 – 3.55 GHz)	25 → 30	N. A.
[23][2023]	Ground plane	4	0.44	0.04	7.2% (3.88 – 4.17 GHz)	22 → 31	N. A.
[25][2024]	Patch layer	5	0.445	0.05	2.4% (4.93 – 5.05 GHz)	11 → 20	N. A.
[26][2021]	Patch layer	5.8	0.5	0.039	1.9% (5.75 – 5.86 GHz)	18 → 20	N. A.
[30][2021]	Patch layer	2.45	0.44	0.049	5.5%*** (2.394 – 2.530 GHz)	5 → 15.4	81.9%–87%
[36][2024]	Patch layer	5.9	0.44	0.065	6.4% (5.74 – 6.12 GHz)	13 → 20	77%–91%
Proposed	**Dielectric layer**	**3.5**	**0.39**	**0.058**	**5.7 % (3.4 – 3.6 GHz)**	**10.6 → 20**	**80%–96%**

*Usable bandwidth: $S_{ii} < -10$ dB and $S_{ij} < -20$ dB.
**Isolation increase: Isolation of minimum improvement within the band: reference → enhanced.
***$S_{ii} < -10$ dB and $S_{ij} < -15$ dB.

patch layer, the ground plane, and the feeding structure. In contrast, the proposed work pioneers a substrate-manipulation method by strategically exploiting dielectric inhomogeneity to suppress strong coupling between two microstrip antennas, thereby offering a new and promising solution in substrate-based decoupling frameworks.

Second, the proposed self-decoupled antenna demonstrates compact element spacing alongside superior operational bandwidth compared to most methods listed in Table II. Moreover, the proposed approach ensures structural simplicity while preserving low-profile properties. Crucially, this work pioneers the integration of 3-D printing with decoupling strategies, whose process flexibility and monolithic fabrication capability enable uneven dielectric distributions within a single substrate. The synergistic fusion of the inhomogeneous substrate manipulation and 3-D printing provides a promising vision for the self-decoupling of microstrip antennas.

Moreover, Table III presents a further comparison with respect to the wideband decoupling methods. As observed, while [49] achieves self-decoupling across a wide bandwidth, it necessitates a stacked patch configuration and larger center-to-center spacing. While [9], [47], [48], and [50] exhibit excellent bandwidth, they typically require additional decoupling structures and generally possess a higher profile. In contrast, the proposed method counteracts multipath coupling by manipulating the permittivity distribution within the substrate. By relying solely on the intrinsic structure of the antenna to achieve high isolation, it yields a comparable bandwidth at the same low profile. This identifies the proposed design as a promising candidate for compact, low-profile, and high-performance antenna arrays.

In addition to the sub-6 GHz applications discussed above, the proposed self-decoupling topology is readily scalable to the millimeter-wave (mm-wave) bands. To demonstrate this applicability, a H-plane 1×2 array operating at 27 GHz

TABLE III
COMPARISON OF THE PROPOSED AND RECENT WIDEBAND MICROSTRIP ANTENNA DECOUPLING TECHNIQUES

Ref.	Self-decoupling	Spacing (λ_0)*	Profile (λ_0)	Usable bandwidth**	Isolation*** (dB)
[9][2024]	No	0.28	0.12	11%	> 15.2
[47][2023]	No	0.283	0.117	17.6%	> 18.9
		0.333	0.1	22.2%	> 19
[48][2021]	No	0.383	0.42	14.0%	> 20
		0.1	0.18	27.3%	
[49][2022]	Yes	0.5	0.07	16.3%	> 20
[50][2025]	No	0.24	0.071	14.1%	> 20
Proposed	**Yes**	**0.394**	**0.077**	**11.6%**	**> 17.5**

*Spacing: the center-to-center spacing.
** Usable bandwidth: $S_{ii} < -10$ dB and $S_{ij} < -20$ dB.
***Isolation: isolation within the –10 dB impedance bandwidth.

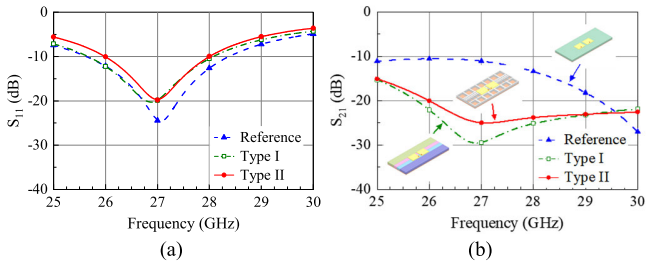

Fig. 22. Simulated S-parameters of the coupled antenna and two proposed mm-wave self-decoupled antennas: Type I and Type II. (a) S_{11}. (b) S_{21}.

was analyzed, with results presented in Figs. 22 and 23. Despite a compact spacing of 0.072 λ_0, the design achieves $S_{11} < -10$ dB and $S_{21} < -20$ dB across the 26–28 GHz band, while maintaining cross-polarization levels below −8.8 dB.

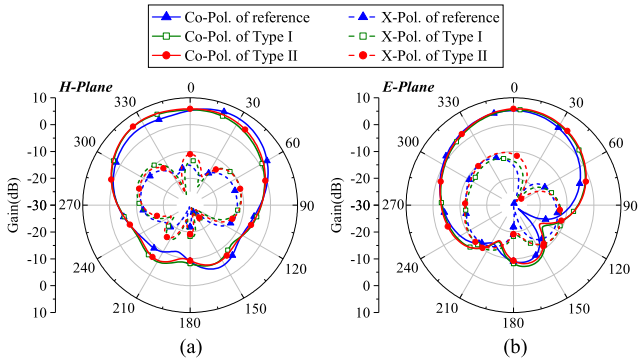

Fig. 23. Simulated radiation patterns of two proposed mm-wave self-decoupled and the coupled antennas at 3.5 GHz. (a) H-plane. (b) E-plane.

Moreover, the proposed method is applicable to 2×2 arrays, which are omitted for conciseness and will be reported in future work.

While miniaturization at higher frequencies increases manufacturing complexity, it is effectively addressed by high-precision AM, such as digital light processing (DLP) with micrometer-level resolution. With 3-D printing and the material production techniques becoming increasingly mature and powerful, the manufacturing complexity issue will become negligible compared to the performance benefits.

V. Conclusion

This work has successfully proposed, developed, and experimentally validated a new and highly efficient approach for achieving self-decoupling in a microstrip antenna through the strategic manipulation of substrate inhomogeneity. The core innovation lies in counteracting multipath coupling by manipulating a specific permittivity distribution within the substrate itself, which is analytically revealed through quantitative formulation. First, a demonstration example with two elements is studied. Both simulated and measured results validate the proposed decoupling scheme, demonstrating over 20 dB isolation and 80%–96% total efficiency across the 3.4–3.6 GHz bandwidth with 0.07 λ_0 edge-to-edge spacing. Besides, the proposed self-decoupling method is also extended to 1×4 array and mm-wave scenarios to justify the generality.

The principal contribution of this article is twofold. First, it is the first known work to achieve antenna self-decoupling primarily through the deliberate manipulation of substrate permittivity inhomogeneity, establishing a new paradigm in decoupling methodology. Second, it pioneers the use of 3-D printing technology for the rapid prototyping and robust fabrication of such complex inhomogeneous dielectric substrates for the self-decoupling of microstrip antennas.

References

[1] K. E. Kolodziej, B. T. Perry, and J. S. Herd, "In-band full-duplex technology: Techniques and systems survey," *IEEE Trans. Microw. Theory Techn.*, vol. 67, no. 7, pp. 3025–3041, Jul. 2019.

[2] X. Chen, S. Zhang, and Q. Li, "A review of mutual coupling in MIMO systems," *IEEE Access*, vol. 6, pp. 24706–24719, 2018.

[3] Y.-M. Zhang, Q.-C. Ye, G. F. Pedersen, and S. Zhang, "A simple decoupling network with filtering response for patch antenna arrays," *IEEE Trans. Antennas Propag.*, vol. 69, no. 11, pp. 7427–7439, Nov. 2021.

[4] X.-J. Zou, G.-M. Wang, Y.-W. Wang, and H.-P. Li, "An efficient decoupling network between feeding points for multielement linear arrays," *IEEE Trans. Antennas Propag.*, vol. 67, no. 5, pp. 3101–3108, May 2019.

[5] J. Sui and K.-L. Wu, "A general T-stub circuit for decoupling of two dual-band antennas," *IEEE Trans. Microw. Theory Techn.*, vol. 65, no. 6, pp. 2111–2121, Jun. 2017.

[6] F. Yang and Y. Rahmat-Samii, "Microstrip antennas integrated with electromagnetic band-gap (EBG) structures: A low mutual coupling design for array applications," *IEEE Trans. Antennas Propag.*, vol. 51, no. 10, pp. 2936–2946, Oct. 2003.

[7] S. Ghosh, T.-N. Tran, and T. Le-Ngoc, "Dual-layer EBG-based miniaturized multi-element antenna for MIMO systems," *IEEE Trans. Antennas Propag.*, vol. 62, no. 8, pp. 3985–3997, Aug. 2014.

[8] B. Qian, X. Huang, X. Chen, M. Abdullah, L. Zhao, and A. Kishk, "Surrogate-assisted defected ground structure design for reducing mutual coupling in 2×2 microstrip antenna array," *IEEE Antennas Wireless Propag. Lett.*, vol. 21, pp. 351–355, 2022.

[9] M. Wang, Z. Shao, M. Tang, Y.-P. Zhang, and J. Mao, "Miniaturization and decoupling of wideband stacked patch antennas based on spoof surface plasmon polaritons," *IEEE Trans. Antennas Propag.*, vol. 72, no. 10, pp. 8076–8081, Oct. 2024.

[10] D. Gao, Z.-X. Cao, S.-D. Fu, X. Quan, and P. Chen, "A novel slot-array defected ground structure for decoupling microstrip antenna array," *IEEE Trans. Antennas Propag.*, vol. 68, no. 10, pp. 7027–7038, Oct. 2020.

[11] T. Pei, L. Zhu, J. Wang, and W. Wu, "A low-profile decoupling structure for mutual coupling suppression in MIMO patch antenna," *IEEE Trans. Antennas Propag.*, vol. 69, no. 10, pp. 6145–6153, Oct. 2021.

[12] H. Qi, L. Liu, X. Yin, H. Zhao, and W. J. Kulesza, "Mutual coupling suppression between two closely spaced microstrip antennas with an asymmetrical coplanar strip wall," *IEEE Antennas Wireless Propag. Lett.*, vol. 15, pp. 191–194, 2016.

[13] M. Xie, X. Wei, Y. Tang, and D. Hu, "A parasitic decoupling structure for dual-polarized patch antenna arrays," *IEEE Antennas Wireless Propag. Lett.*, vol. 22, pp. 1351–1355, 2023.

[14] K.-L. Wu, C. Wei, X. Mei, and Z.-Y. Zhang, "Array-antenna decoupling surface," *IEEE Trans. Antennas Propag.*, vol. 65, no. 12, pp. 6728–6738, Dec. 2017.

[15] C. Wei, Z.-Y. Zhang, and K.-L. Wu, "Phase compensation for decoupling of large-scale staggered dual-polarized dipole array antennas," *IEEE Trans. Antennas Propag.*, vol. 68, no. 4, pp. 2822–2831, Apr. 2020.

[16] F. Liu, J. Guo, L. Zhao, G.-L. Huang, Y. Li, and Y. Yin, "Dual-band metasurface-based decoupling method for two closely packed dual-band antennas," *IEEE Trans. Antennas Propag.*, vol. 68, no. 1, pp. 552–557, Jan. 2020.

[17] P. Mondal, D. Dhara, and A. R. Harish, "A partially reflective FSS-based superstrate as a decoupling structure for reducing the mutual coupling of circularly polarized antennas," *IEEE Trans. Antennas Propag.*, vol. 72, no. 4, pp. 3652–3661, Apr. 2024.

[18] M. Li, B. G. Zhong, and S. W. Cheung, "Isolation enhancement for MIMO patch antennas using near-field resonators as coupling-mode transducers," *IEEE Trans. Antennas Propag.*, vol. 67, no. 2, pp. 755–764, Feb. 2019.

[19] A. Jafargholi, A. Jafargholi, and J. H. Choi, "Mutual coupling reduction in an array of patch antennas using CLL metamaterial superstrate for MIMO applications," *IEEE Trans. Antennas Propag.*, vol. 67, no. 1, pp. 179–189, Jan. 2019.

[20] Z. Qamar, U. Naeem, S. A. Khan, M. Chongcheawchamnan, and M. F. Shafique, "Mutual coupling reduction for high-performance densely packed patch antenna arrays on finite substrate," *IEEE Trans. Antennas Propag.*, vol. 64, no. 5, pp. 1653–1660, May 2016.

[21] D. P. Purbey, S. Ghosal, and A. De, "Shorting-pin-inspired coupling reduction in dual-band dual-polarized STAR antenna," *IEEE Antennas Wireless Propag. Lett.*, vol. 24, pp. 43–47, 2025.

[22] H. Lin, Q. Chen, Y. Ji, X. Yang, J. Wang, and L. Ge, "Weak-field-based self-decoupling patch antennas," *IEEE Trans. Antennas Propag.*, vol. 68, no. 6, pp. 4208–4217, Jun. 2020.

[23] Q. X. Lai, Y. M. Pan, and S. Y. Zheng, "A self-decoupling method for MIMO antenna array using characteristic mode of ground plane," *IEEE Trans. Antennas Propag.*, vol. 71, no. 3, pp. 2126–2135, Mar. 2023.

[24] J. Wu, C. Tong, N. Yang, K. W. Leung, K. Lu, and P. Hu, "Radiation pattern decoupled patch antennas based on TM_{01} and TM_{11} modes," *IEEE Antennas Wireless Propag. Lett.*, vol. 22, pp. 2695–2699, 2023.

[25] L. Zha, Y. M. Pan, and S. Y. Zheng, "Self-decoupled linear and planar MIMO microstrip patch antenna arrays operating in the fundamental TM01 mode," *IEEE Trans. Antennas Propag.*, vol. 72, no. 2, pp. 1224–1233, Feb. 2024.
[26] Q. X. Lai, Y. M. Pan, S. Y. Zheng, and W. J. Yang, "Mutual coupling reduction in MIMO microstrip patch array using TM_{10} and TM_{02} modes," *IEEE Trans. Antennas Propag.*, vol. 69, no. 11, pp. 7562–7571, Nov. 2021.
[27] P. Kim-Thi, T. N. Van, and T. B. Thanh, "A self-decoupling technique for isolation enhancement in closely-spaced MIMO patch antennas," *IEEE Antennas Wireless Propag. Lett.*, vol. 23, pp. 1695–1699, 2024.
[28] J. Xu, X. He, and T. Deng, "A self-decoupled MIMO patch array with consistent radiation patterns," *IEEE Trans. Antennas Propag.*, vol. 72, no. 12, pp. 8971–8979, Dec. 2024.
[29] Y. Wang, Q. Xue, and H. Xie, "Wideband decoupled asynchronously coupled patch antennas," *IEEE Trans. Antennas Propag.*, vol. 73, no. 2, pp. 906–919, Feb. 2024.
[30] L. Sun, Y. Li, and Z. Zhang, "Decoupling between extremely closely spaced patch antennas by mode cancellation method," *IEEE Trans. Antennas Propag.*, vol. 69, no. 6, pp. 3074–3083, Jun. 2021.
[31] Y.-Z. Liang, F.-C. Chen, K.-R. Xiang, and W.-F. Zeng, "Wideband co-polarized stacked patch antenna for in-band full-duplex applications," *IEEE Trans. Antennas Propag.*, vol. 71, no. 12, pp. 9920–9925, Dec. 2023.
[32] A. Zhang, K. Wei, Y. Hu, and Q. Guan, "High-isolated coupling-grounded patch antenna pair with shared radiator for the application of 5G mobile terminals," *IEEE Trans. Antennas Propag.*, vol. 70, no. 9, pp. 7896–7904, Sep. 2022.
[33] Y.-F. Cheng and K.-K.-M. Cheng, "Decoupling of 2×2 MIMO antenna by using mixed radiation modes and novel patch element design," *IEEE Trans. Antennas Propag.*, vol. 69, no. 12, pp. 8204–8213, Dec. 2021.
[34] M. Li, S. Tian, M.-C. Tang, and L. Zhu, "A compact low-profile hybrid-mode patch antenna with intrinsically combined self-decoupling and filtering properties," *IEEE Trans. Antennas Propag.*, vol. 70, no. 2, pp. 1511–1516, Feb. 2022.
[35] Y. Peng, J. Sui, D. Li, J. Li, and X. Zhu, "Wideband co-linearly polarized microstrip antenna for in-band full-duplex systems using two parallel L-probes," *IEEE Antennas Wireless Propag. Lett.*, vol. 23, pp. 4603–4607, 2024.
[36] J. Qian, B. S. Izquierdo, S. Gao, H. Wang, H. Zhou, and H. Xu, "A novel low-cost H-plane decoupling technique for two closely placed patch antennas using electric and magnetic coupling cancellation," *IEEE Trans. Antennas Propag.*, vol. 72, no. 5, pp. 3864–3873, May 2024.
[37] S. Wang, L. Zhu, and W. Wu, "3-D printed inhomogeneous substrate and superstrate for application in dual-band and dual-CP stacked patch antenna," *IEEE Trans. Antennas Propag.*, vol. 66, no. 5, pp. 2236–2244, May 2018.
[38] S. Wang, X. Zhang, L. Zhu, and W. Wu, "Single-fed wide-beamwidth circularly polarized patch antenna using dual-function 3-D printed substrate," *IEEE Antennas Wireless Propag. Lett.*, vol. 17, pp. 649–653, 2018.
[39] G. Muntoni et al., "A curved 3-D printed microstrip patch antenna layout for bandwidth enhancement and size reduction," *IEEE Antennas Wireless Propag. Lett.*, vol. 19, pp. 1118–1122, 2020.
[40] J. Wu, A. H. Abdelrahman, M. Liang, X. Yu, and H. Xin, "Monopole antenna radiation pattern control via 3-D-printed dielectrics," *IEEE Trans. Antennas Propag.*, vol. 65, no. 8, pp. 3869–3876, Aug. 2017.
[41] A. Petosa and A. Ittipiboon, "Design and performance of a perforated dielectric Fresnel lens," *IEE Proc. Microw., Antennas Propag.*, vol. 150, no. 5, pp. 309–314, Oct. 2003.
[42] M. Imbert, A. Papio, F. De Flaviis, L. Jofre, and J. Romeu, "Design and performance evaluation of a dielectric flat lens antenna for millimeter-wave applications," *IEEE Antennas Wireless Propag. Lett.*, vol. 14, pp. 342–345, 2015.
[43] L. Sun, Y. Li, Z. Zhang, and H. Wang, "Antenna decoupling by common and differential modes cancellation," *IEEE Trans. Antennas Propag.*, vol. 69, no. 2, pp. 672–682, Feb. 2021.
[44] Y.-X. Zhang, Y.-C. Jiao, and L. Zhang, "Wideband inhomogeneous-polarizer loaded circularly polarized SIW horn antenna for broadband millimeter-wave applications," *IEEE Antennas Wireless Propag. Lett.*, vol. 18, pp. 1448–1452, 2019.
[45] J. M. Monkevich and G. P. Le Sage, "Design and fabrication of a custom-dielectric Fresnel multi-zone plate lens antenna using additive manufacturing techniques," *IEEE Access*, vol. 7, pp. 61452–61460, 2019.
[46] M. M. Nikolic, A. R. Djordjevic, and A. Nehorai, "Microstrip antennas with suppressed radiation in horizontal directions and reduced coupling," *IEEE Trans. Antennas Propag.*, vol. 53, no. 11, pp. 3469–3476, Nov. 2005.
[47] L. Ma, Z. Shao, J. Lai, C. Gu, and J. Mao, "A compact dual-decoupling scheme for aperture-coupled and probe-fed closely spaced wideband microstrip antennas," *IEEE Trans. Antennas Propag.*, vol. 71, no. 11, pp. 9072–9077, Nov. 2023.
[48] M. Li, M. Y. Jamal, L. Jiang, and K. L. Yeung, "Isolation enhancement for MIMO patch antennas sharing a common thick substrate: Using a dielectric block to control space-wave coupling to cancel surface-wave coupling," *IEEE Trans. Antennas Propag.*, vol. 69, no. 4, pp. 1853–1863, Apr. 2021.
[49] Y. Fang, L.-S. Wu, L.-F. Qiu, and Y. P. Zhang, "A method of introducing coupling null by shorting pins for stacked microstrip patch antenna array," *IEEE Trans. Antennas Propag.*, vol. 70, no. 7, pp. 6030–6035, Jul. 2022.
[50] J. Shi, Y. He, R. Shi, J. Geng, and H. Sun, "Wideband decoupling for tightly placed stacked patch antenna based on lumped and distributed elements," *IEEE Antennas Wireless Propag. Lett.*, vol. 24, pp. 2064–2068, 2025.

Yongqi Hu (Graduate Student Member, IEEE) was born in Shantou, China, in 2001. She received the B.S. degree in electronic information science and technology from Sun Yat-sen University, Shenzhen, China, in 2024, where she is currently pursuing the M.S. degree with the School of Electronics and Communication Engineering.

Her current research interests include microstrip patch antennas, 5G terminal antenna design, and 3-D printing technology.

Jiangwei Sui (Member, IEEE) received the B.S. degree from the University of Science and Technology of China, Hefei, China, in 2014, and the Ph.D. degree from The Chinese University of Hong Kong, Hong Kong, China, in 2019.

From 2019 to 2020, he was with Vivo Mobile Communication Company Ltd., Dongguan, China, as an Antenna Engineer. Since 2021, he has been with the School of Electronics and Communication Engineering, Sun Yat-sen University, Shenzhen, China, where he is currently an Associate Professor. His current research interests include antenna theory and design, especially the MIMO antenna technology and associated antenna decoupling techniques for mobile devices, base stations, and navigation systems.

Xiangwei Zhu (Member, IEEE) received the M.S. degree in communication engineering and the Ph.D. degree in information and communication engineering from the College of Electronic Science and Engineering, National University of Defense Technology, Changsha, China, in 2003 and 2007, respectively.

He is currently a Professor with the College of Electronics and Communication Engineering, Sun Yat-sen University, Shenzhen, China. His current research interests include Beidou satellite navigation, new navigation communication microwave devices, and intelligent cognitive navigation.